Microscopic study of the deformed neutron halo of ^{31}Ne

R. Takatsu
Department of Physics, Hokkaido University, Sapporo 060-0810, Japan

Y. Suzuki
Research Center for Nuclear Physics (RCNP), Osaka University, Ibaraki 567-0047, Japan

W. Horiuchi*
Department of Physics, Osaka Metropolitan University, Osaka 558-8585, Japan;
Nambu Yoichiro Institute of Theoretical and Experimental Physics (NITEP), Osaka Metropolitan University, Osaka 558-8585, Japan;
and RIKEN Nishina Center, Wako 351-0198, Japan, and Department of Physics, Hokkaido University, Sapporo 060-0810, Japan

M. Kimura†
RIKEN Nishina Center, Wako 351-0198, Japan, and Department of Physics, Hokkaido University, Sapporo 060-0810, Japan

(Received 1 December 2022; accepted 13 February 2023; published 27 February 2023)

The properties of the deformed halo of ^{31}Ne are discussed using the antisymmetrized molecular dynamics plus resonating group method (AMD+RGM). The AMD+RGM calculations describe a large neutron radius for the ground state and reveal that the ground state is dominated by core-excited components. The resonant states are also investigated by applying the analytical continuation of the coupling constant. It is found that the first excited state (the $5/2^-$ state) is also dominated by core-excited components and has a small decay width, whereas the second excited state (the $7/2^-$ state) is dominated by the valence neutron in the f wave coupled to the ground state of ^{30}Ne.

DOI: 10.1103/PhysRevC.107.024314

I. INTRODUCTION

The formation of a neutron halo with a broad neutron distribution outside the core nucleus is a unique phenomenon observed near the drip line [1]. Since their first discovery in ^{11}Li [2], neutron haloes have been observed and discussed up to sd-pf shell regions, such as ^{22}C, ^{29}F, and ^{37}Mg [3–8]. ^{31}Ne is one such example whose large nuclear radius has been reported from the measurement of interaction [9] and Coulomb breakup [10,11] cross sections. Note that in the normal shell ordering of spherical potentials, the valence neutron of ^{31}Ne occupies $f_{7/2}$; however, it must occupy the s or p wave to form the neutron halo [12]. Thus, the shell structure of ^{31}Ne is modified from the normal one. This change in shell order is ascribed to deformation. Hamamoto investigated the properties of neutron orbits based on the Nilsson model (a deformed Woods-Saxon potential) to explain the observed large Coulomb dissociation cross section, and noted that the valence neutron likely occupies particular orbits ([330 1/2], [321 3/2], or [200 1/2]) [13]. In these cases, the ground state is either $J^\pi = 3/2^-$ or $1/2^+$. This result is consistent with shell model calculations [10,11,14] and particle-rotor model calculations [15,16]; however, to understand the structure of the deformed halo, it is important to investigate this with a full microscopic model that can describe the halo structure.

In a previous work [17–19], the antisymmetrized molecular dynamics plus resonating group method (AMD+RGM) framework was applied to describe the spatially extended halo structure and was combined with a microscopic nuclear reaction model to discuss the large interaction cross-section of ^{31}Ne. In the present study, we focus on the details of this structure calculation and discuss the properties of the deformed halo of ^{31}Ne. We show that the ground state of ^{31}Ne is dominated by core-excited components, indicating the strong coupling between the deformed halo and rotational excitation of the core nucleus. However, the AMD+RGM approach is inaccurate for describing resonance states. To overcome this problem, in this study, we introduce the method of the analytical continuation of the coupling constant (ACCC) [20,21]. We demonstrate that the combination of the AMD+RGM and ACCC is successful in determining the energies and widths of resonances. The first excited state, the $5/2^-_1$ state, is dominated by the core-excited components, whereas the second excited state, the $7/2^-_1$ state, is not.

This paper is organized as follows: In the next section, we explain the theoretical frameworks, that is, the AMD+GCM, AMD+RGM, and ACCC, which are used to describe ^{31}Ne. In Sec. III, we compare the antisymmetrized molecular dynamics plus generator coordinate method (AMD+GCM) and AMD+RGM results and discuss the deformed neutron halo.

*whoriuchi@omu.ac.jp
†masaaki.kimura@riken.jp

Based on the ACCC, we also discuss the excited resonant states built on top of the deformed halo. The final section summarizes this study.

II. THEORETICAL FRAMEWORK

In this study, we apply the AMD+GCM and AMD+RGM frameworks to describe the neutron halo of ^{31}Ne. The Hamiltonian is common in both frameworks and is given as

$$H = \sum_{i=1}^{A} t_i + \sum_{i<j}^{A} v_{ij} - t_{\text{c.m.}}, \tag{1}$$

where the Gogny D1S interaction [22] is used as effective nucleon-nucleon and Coulomb interactions. The center-of-mass kinetic energy, $t_{\text{c.m.}}$, is exactly removed.

The variational wave function is also common; a parity-projected Slater determinant of single-particle Gaussian wave packets are employed.

$$\Phi^{\pi}_{\text{int}} = \frac{1+\pi P_x}{2}\mathcal{A}\{\varphi_1\varphi_2\dots\varphi_A\}, \tag{2}$$

where P_x is the parity operator. In this study, we focus on the positive-parity states ($\pi = +1$) of ^{30}Ne and the negative-parity states ($\pi = -1$) of ^{31}Ne. A single-particle wave packet has a deformed Gaussian form [23],

$$\varphi_i(\mathbf{r}) = \prod_{\sigma=x,y,z} \exp\{-\nu_\sigma(r_\sigma - Z_{i\sigma})^2\}\chi_i\eta_i, \tag{3}$$

where χ_i is the spinor and η_i is the isospin fixed to either a proton or neutron. The parameters of the variational wave function are $\boldsymbol{Z}_i$, $\boldsymbol{\nu}$, and χ_i.

A. AMD+GCM

The parameters of the variational wave function are optimized by the energy variation with the constraint on the nuclear quadrupole deformation parameter β. After energy variation, we obtain the optimized wave functions $\Phi^{\pi}_{\text{int}}(\beta)$ for each given value of β. The optimized wave functions are projected on the eigenstates of the total angular momentum,

$$\begin{aligned}\Phi^{J\pi}_{\text{MK}}(\beta) &= P^{J}_{\text{MK}}\Phi^{\pi}_{\text{int}}(\beta)\\ &= \frac{2J+1}{8\pi^2}\int d\Omega D^{J*}_{\text{MK}}(\Omega)R(\Omega)\Phi^{\pi}_{\text{int}}(\beta),\end{aligned} \tag{4}$$

where P^{J}_{MK}, $D^{J}_{\text{MK}}(\Omega)$, and $R(\Omega)$ denote the angular momentum projector, Wigner D function, and rotation operator, respectively. Then, we superpose the wave functions with different values of the quadrupole deformation parameter β,

$$\Psi^{J\pi}_{M\alpha} = \sum_{Ki} e_{Ki\alpha}\Phi^{J\pi}_{\text{MK}}(\beta_i). \tag{5}$$

The coefficients $e_{Ki\alpha}$ can be obtained from the Hill-Wheeler equation [24],

$$\sum_{K'i'}(H_{KiK'i'} - E_\alpha N_{KiK'i'})e_{K'i'\alpha} = 0, \tag{6}$$

$$H_{KiK'i'} = \left\langle \Phi^{J\pi}_{\text{MK}}(\beta_i)\middle|H\middle|\Phi^{J\pi}_{\text{MK}'}(\beta_{i'})\right\rangle, \tag{7}$$

$$N_{KiK'i'} = \left\langle \Phi^{J\pi}_{\text{MK}}(\beta_i)|\Phi^{J\pi}_{\text{MK}'}(\beta_{i'})\right\rangle, \tag{8}$$

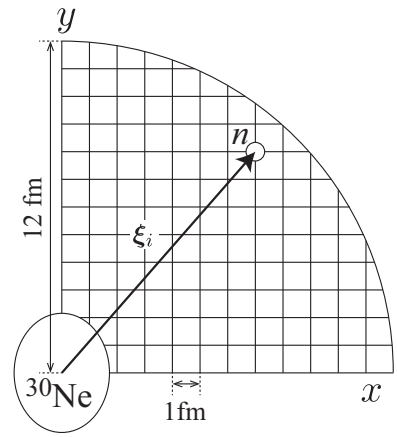

FIG. 1. Schematic illustration of an AMD+RGM basis wave function for the ^{30}Ne $+n$ system.

where E_α is the eigenenergy of the eigenfunction given by Eq. (5).

This AMD+GCM framework has often been used for nuclear structure calculations [25–27]; however, it has a disadvantage in describing neutron haloes because the asymptotics of the wave function are restricted to a Gaussian form. To overcome this problem, we apply the AMD+RGM framework to ^{31}Ne.

B. AMD+RGM and ACCC

In the AMD+RGM framework [18,28], we introduce an additional set of wave functions that covers a large distance from the core nucleus. As schematically illustrated in Fig. 1, we construct ^{30}Ne $+n$ wave functions, which consist of ^{30}Ne and a valence neutron located on a grid inside a 12-fm radius sphere with 1-fm intervals,

$$\Phi(\beta, \boldsymbol{\xi}_i, \chi_n) = \mathcal{A}\left\{\Phi_{^{30}\text{Ne}}\left(\beta, -\tfrac{1}{31}\boldsymbol{\xi}_i\right)\varphi_n\left(\tfrac{30}{31}\boldsymbol{\xi}_i, \chi_n\right)\right\}, \tag{9}$$

where $\Phi_{^{30}\text{Ne}}$ is the intrinsic wave function of ^{30}Ne, obtained from the energy variation with the constraint on β, and φ_n is a Gaussian wave packet [Eq. (3)], which describes the valence neutron. To reduce the computational cost, we assume axial and reflection symmetry for $\Phi_{^{30}\text{Ne}}$. Hence, the relative coordinate $\boldsymbol{\xi}_i$ between ^{30}Ne and the valence neutron is restricted within the first quadrant of the xy plane, where the y axis was the symmetry axis of $\Phi_{^{30}\text{Ne}}$. The generated basis functions are superposed with the basis functions obtained via the variational calculations,

$$\begin{aligned}\Psi^{J\pi}_{M\alpha} = \sum_K \Bigg\{ &\sum_{i=1} f_{Ki\alpha}\Phi^{J\pi}_{\text{MK}}(\beta_i)\\ &+ \sum_{ij}\sum_{\chi_n=\uparrow,\downarrow} g_{Kij\chi_n\alpha}P^{J}_{\text{MK}}P^{\pi}\Phi(\beta_i, \boldsymbol{\xi}_j, \chi_n)\Bigg\}.\end{aligned} \tag{10}$$

Similar to the AMD+GCM framework, the coefficients $f_{Ki\alpha}$ and $g_{Kij\chi_n\alpha}$ and the eigenenergy are determined from the Hill-Wheeler equation.

The AMD+RGM framework [18,28] can describe a long-ranged halo wave function; however, it is difficult to identify the resonances owing to the strong coupling with nonresonant continua. Therefore, we apply the ACCC [20,21] to calculate the energies and widths of the resonances. We use the two-body spin-orbit interaction of the Gogny D1S functional as an auxiliary potential,

$$H(\lambda) = H + \lambda v_{ls}, \tag{11}$$

$$v_{ls} = iW_{ls}(\overrightarrow{\sigma_1} + \overrightarrow{\sigma_2}) \cdot \overleftarrow{\nabla} \times \delta^3(\boldsymbol{r}_1 - \boldsymbol{r}_2)\overrightarrow{\nabla}, \tag{12}$$

where λ controls the strength of the auxiliary potential, and $\lambda = 0$ corresponds to the physical point, that is, the original Hamiltonian. We note that this auxiliary potential is the same as the standard form of the spin-orbit interaction of the Gogny and Skyrme density functionals [22,29]. Hence, the addition of the above spin-orbit term is equivalent to multiplying a factor of $1 + \lambda$ to the original spin-orbit interaction.

We also comment on the choice of the auxiliary potentials. In general, its choice is arbitrary; a typical choice is the spin- and isospin-dependent central force. We also tested such a case and found that it did not work for ^{31}Ne. The use of the central auxiliary potential largely changed the binding energies and structure of ^{30}Ne and ^{31}Ne in the bound state region from those at the physical point with $\lambda = 0$. Consequently, the extrapolation by the Páde approximation was less accurate. Therefore, in the present study, we show the properties of the resonances obtained by using the spin-orbit auxiliary field.

The eigenenergy of ^{31}Ne derived from this Hamiltonian, which we denote as $E(\lambda)$, varies as a function of λ. For larger values of λ, resonances are bound owing to the additional attraction from the auxiliary potential, whereas nonresonant states are insensitive to it. In such a way, we can distinguish resonances from nonresonant continua. The energy and width of a resonance can be calculated by the analytical continuation of the eigenenergy $E(\lambda)$ from the bound region to the physical point. To this end, we introduced a variable X,

$$X = \sqrt{\lambda - \lambda_0}, \tag{13}$$

where λ_0 is the value at which an eigenstate of ^{31}Ne becomes particle unbound, i.e., let $E_{^{30}\mathrm{Ne}}(\lambda_0)$ be the energy of the ground state of ^{30}Ne calculated from $H(\lambda)$, and λ_0 satisfies $E(\lambda_0) = E_{^{30}\mathrm{Ne}}(\lambda_0)$. Using X, the wave number of the valence neutron is approximated by a fractional function (the Padé approximation),

$$E(\lambda) = \frac{\hbar^2}{2\mu}k^2(X) + E_{^{30}\mathrm{Ne}}(\lambda), \tag{14}$$

$$k(X) = i\frac{c_1X + \cdots + c_MX^M}{1 + d_1X + \cdots + d_NX^N}, \tag{15}$$

where μ is the reduced mass of the two-body system. The $N + M$ coefficients are determined by fitting the eigenvalue $E(\lambda)$ in the bound region. In this study, $N = M = 7$ is found to be sufficient for accurate approximation. Then, the wave number at the physical point, $X_0 = i\sqrt{\lambda_0}$, corresponds to the energy and width of resonance as $\hbar^2k^2(X_0)/(2\mu) = E_R - i\Gamma_R/2$.

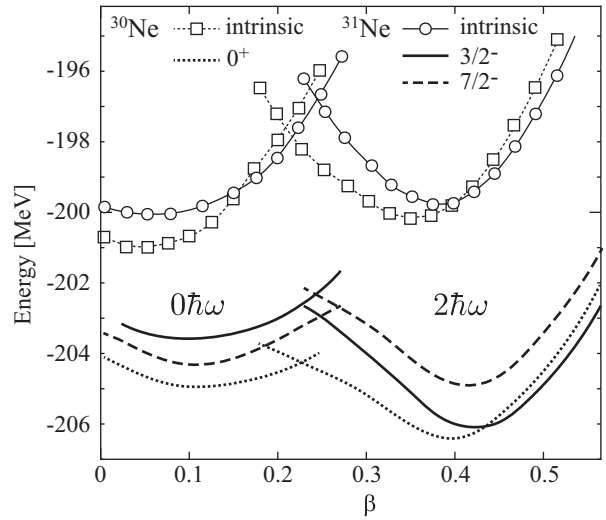

FIG. 2. Energy curves of ^{30}Ne and ^{31}Ne obtained from β-constrained variational calculations.

C. Valence neutron wave function

To investigate the valence neutron wave functions, we calculate the overlap integral between the AMD+GCM wave function of ^{30}Ne and the AMD+GCM or AMD+RGM wave function of ^{31}Ne,

$$\psi(\boldsymbol{r}) = \sqrt{31}\langle\Psi_M^{J^\pi}(^{30}\mathrm{Ne})\big|\Psi_{M+m}^{J'^{\pi'}}(^{31}\mathrm{Ne})\rangle. \tag{16}$$

The computational method for this integral is explained in Ref. [30]. The multipole decomposition of Eq. (16) can be expressed as

$$\psi(\boldsymbol{r}) = \sum_{jl} C_{JMjm}^{J'M+m} u_{jl}(r)/r[Y_l(\hat{r}) \otimes \chi]_{jm}, \tag{17}$$

where $C_{JMjm}^{J'M+m}$ is the Clebsch-Gordan coefficient. Here, $u_{jl}(r)$ is regarded as the valence neutron wave function coupled to the ^{30}Ne core with a spin parity of J^π. The squared integral of $u_{jl}(r)$ is the spectroscopic factor (S factor),

$$S_{jl} = \int_0^\infty dr\, |u_{jl}(r)|^2. \tag{18}$$

III. RESULTS AND DISCUSSION

A. AMD+GCM results

Figure 2 shows the energy curves of ^{30}Ne and ^{31}Ne obtained from β-constrained variational calculations. Both nuclei exhibit energy minima at approximately $\beta = 0.1$ and 0.4. As shown later, these minima correspond to the $0\hbar\omega$ and $2\hbar\omega$ configurations, respectively. The energies of the $0\hbar\omega$ and $2\hbar\omega$ configurations are inverted near $\beta = 0.25$. To explain the structure of the $0\hbar\omega$ and $2\hbar\omega$ configurations, Fig. 3(a) shows the single-particle energies of the last five neutrons of ^{31}Ne. In the $0\hbar\omega$ configuration ($\beta < 0.25$), the last neutron occupies the [330 1/2] Nilsson orbit originating from the spherical $f_{7/2}$. In other words, the $0\hbar\omega$ configuration has one particle and zero holes (1p0h) with respect to the $N = 20$ shell closure. In the $2\hbar\omega$ configuration ($\beta > 0.25$), there are

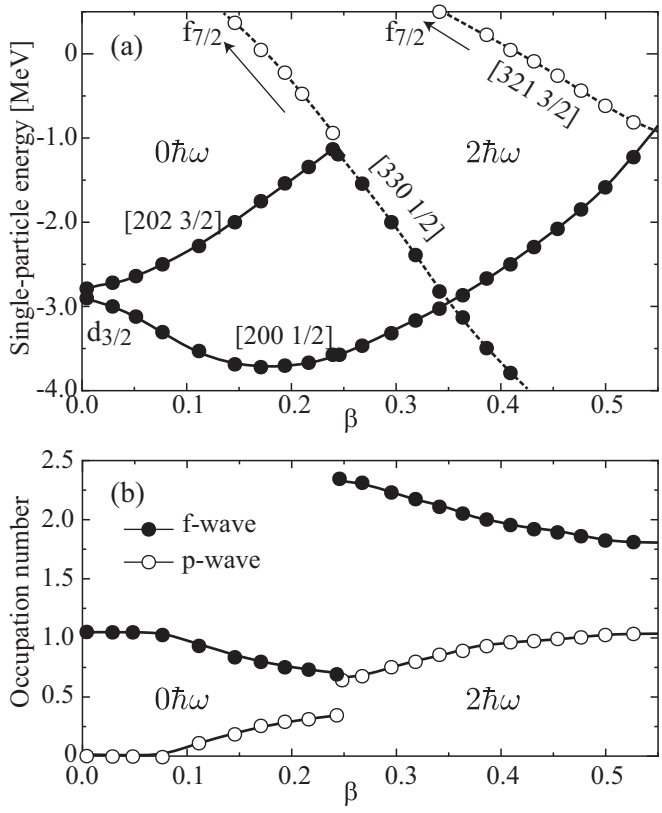

FIG. 3. (a) Single-particle energies of the five most weakly bound neutrons. Only the occupied orbits are calculated in the AMD+GCM framework. (b) Occupation numbers of the p and f waves from the five most weakly bound neutrons.

two neutrons in the [330 1/2] orbit and one in the [321 3/2] orbit, which is another intruder orbit from $f_{7/2}$. Because the [202 3/2] orbit is unoccupied, the $2\hbar\omega$ configuration corresponds to 3p2h. At larger deformations ($\beta > 0.6$), the 4p3h configuration appears, in which two neutrons occupy the [321 3/2] orbit and the last neutron occupies the [200 1/2] orbit, although it is not shown because of its higher excitation energy. These three configurations (1p0h, 3p2h, and 4p3h) are in agreement with the analysis by Hamamoto [13].

Note that these single-particle orbits are not the eigenstates of the orbital angular momentum but mixed states due to deformation. More specifically, the intruder orbits from the spherical $f_{7/2}$ orbit ([330 1/2] and [321 3/2]) are the admixture of f and p waves. The occupation numbers of the f and p waves in these intruder orbits are shown in Fig. 3(b). They discontinuously change at $\beta = 0.25$ because the configuration switches from the $0\hbar\omega$ to $2\hbar\omega$. The sum of the occupation numbers of the f and p waves is approximately one or three, corresponding to 1p0h and 3p2h. If β is close to zero, the last neutron mostly occupies the spherical $f_{7/2}$ orbit, and hence, the occupation number of the p wave is almost zero. As deformation increases, the occupation number of the p wave gradually increases. The ground state of ^{31}Ne approximately corresponds to $\beta = 0.45$, where the occupation numbers of the p and f waves are approximately one and two, respectively.

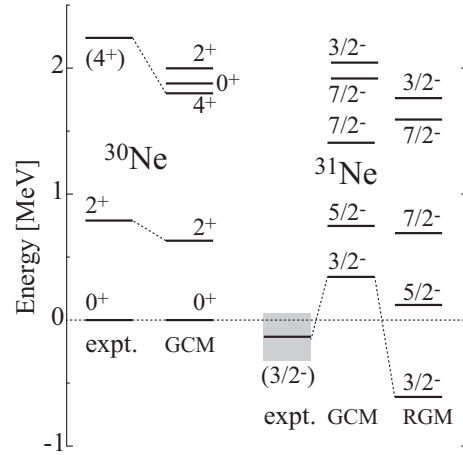

FIG. 4. Energy spectrum of ^{30}Ne and ^{31}Ne relative to the ground state of ^{30}Ne. The AMD+GCM results are denoted as "GCM" and the AMD+RGM results as "RGM."

After the angular momentum projection, the energy of the $2\hbar\omega$ minimum is lower than that of the $0\hbar\omega$ minimum for both nuclei, indicating that the ground state is dominated by the $2\hbar\omega$ configuration. Here, we focus on the energy curve of ^{31}Ne. For the $0\hbar\omega$ configuration, the $7/2^-$ state is lower than the $3/2^-$ state, indicating that the spherical $f_{7/2}$ orbit is lower than the $p_{3/2}$ orbit in accordance with the normal shell order. It is noted that the energy difference between the $7/2^-$ and $3/2^-$ states with the $0\hbar\omega$ configuration is less than 1 MeV, which indicates the quenching of the spherical $N = 28$ shell gap. For the largely deformed $2\hbar\omega$ configuration, the $3/2^-$ state is lower than the $7/2^-$ state because the valence neutron occupies the Nilsson orbit [321 3/2] and generates rotational states with $K^\pi = 3/2^-$.

The comparison of the three configurations proposed by Hamamoto [13] can be summarized as follows. The 1p0h configuration ([330 1/2]): Our calculations do not yield a rotational spectrum because of the small deformation and the spin parity of the ground state is $7/2^-$, which cannot have the halo structure. The 3p2h configuration ([321 3/2]): This yields a rotational spectrum with $K^\pi = 3/2^-$ and can explain the halo structure of ^{31}Ne. The 4p3h configuration ([200 1/2]): The energy of this configuration has excitation energy that is too large and cannot be the ground state if we attempt to consistently reproduce the properties of the neighboring nuclei. Thus, 3p2h is the primary candidate for the ground-state configuration.

Figure 4 shows the spectra of ^{30}Ne and ^{31}Ne obtained from AMD+GCM. ^{30}Ne is largely deformed and has the rotational ground band that consists of the 0_1^+, 2_1^+, and 4_1^+ states. Our calculation predicts the 0_2^+ and 2_2^+ states with $0\hbar\omega$ configuration at approximately 2 MeV, although they have not yet been experimentally identified. The ground state of ^{31}Ne is also dominated by the $2\hbar\omega$ configuration, which exhibits a rotational spectrum with $K^\pi = 3/2^-$ owing to large deformation. An obvious problem in the AMD+GCM calculations is that ^{31}Ne is unbound, and hence, we apply the

TABLE I. One-neutron separation energy in units of MeV (S_n), point-proton and neutron distribution radii in units of fm, and the quadrupole moments of protons (Q_p) and neutrons (Q_n) in units of fm^2. The AMD+GCM results are denoted as "GCM" and the AMD+RGM results as "RGM."

	S_n	$\sqrt{\langle r_p^2\rangle}$	$\sqrt{\langle r_n^2\rangle}$	Q_p	Q_n
^{30}Ne(GCM)		3.05	3.40		
^{31}Ne(GCM)	−0.36	3.06	3.45	11.8	29.1
^{31}Ne(RGM)	0.61	3.11	3.69	11.2	31.1

AMD+RGM and ACCC frameworks to improve the description of neutron haloes.

B. AMD+RGM and ACCC results

Here, we show how the AMD+RGM calculation improves the description of the neutron halo and bound the ground state of ^{31}Ne. As listed in Table I, the calculated one-neutron separation energy (S_n) is 610 keV, which is approximately 1 MeV deeper than the AMD+GCM result and slightly overestimats the experimental value of 150 ± 160 keV deduced from the one-neutron removal experiment [11]. The neutron distribution radius has increased from 3.45 fm in the AMD+GCM to 3.69 fm in the AMD+RGM owing to the proper description of the neutron halo. The proton radius has also increased slightly owing to the recoil effect of the valence neutron.

The large electric quadrupole moment predicted by the present calculations is a direct observable to show core deformation. The quadrupole moment of neutrons is also large and slightly larger in the AMD+RGM result than in the AMD+GCM result because of the development of the p-wave neutron halo with spatial anisotropy.

To discuss the structure of the deformed halo in more detail, the spectroscopic factors of the ground state are listed in Table II. The main channels of the ground state are $J^\pi \otimes l_j = 0_1^+ \otimes p_{3/2}$, $2_1^+ \otimes p_{3/2}$, $2_1^+ \otimes f_{7/2}$, and $4_1^+ \otimes f_{7/2}$, where J^π is the spin parity of ^{30}Ne, and l_j is the angular momentum of the valence neutron. Compared with the AMD+GCM results, the S factors of the p-wave channels have increased in the AMD+RGM results owing to the formation of a p-wave halo. The one-neutron removal experiment reported the S factor of the $0_1^+ \otimes p_{3/2}$ channel as 0.32 ± 0.21 [11], which is reasonably reproduced by the AMD+RGM calculation. It is remarkable that AMD+RGM calculations yields larger S factors for core-excited channels ($2_1^+ \otimes p_{3/2}$, $2_1^+ \otimes f_{7/2}$, and $4_1^+ \otimes f_{7/2}$) than the $0_1^+ \otimes p_{3/2}$ channel because of the strong coupling between the neutron halo and the rotational excitation of the deformed core. This is qualitatively consistent with the results of the rigid-rotor model calculation [15], which assumed large core deformation, and the shell model calculation with the SDPF-M interaction [11]. In fact, the observed inclusive parallel momentum distribution for the $1n$-removal reaction [11] showed that the f-wave component is larger than the p-wave component, which is consistent with the theoretical calculations. Whether the reaction calculation can reproduce this momentum distribution is an interesting problem for future study.

Figure 5 compares the wave functions of the valence neutron (overlap integral of ^{31}Ne and ^{30}Ne) in the $J^\pi \otimes l_j = 0_1^+ \otimes p_{3/2}$, $2_1^+ \otimes p_{3/2}$, and $2_1^+ \otimes f_{7/2}$ channels calculated using the AMD+GCM and AMD+RGM. The AMD+RGM has significantly improved the description of the wave function in all channels and has reproduced the correct asymptotics at large distances. The neutron wave function in the $0_1^+ \otimes p_{3/2}$ channel exhibits a very long tail due to the small S_n and small orbital angular momentum, which is the origin of the large neutron halo. The wave function of the $2_1^+ \otimes p_{3/2}$ channel also exhibits a similar distribution; however, it dumps more quickly than that of the $0_1^+ \otimes p_{3/2}$ channel because core excitation enlarges S_n. The $2_1^+ \otimes f_{7/2}$ channel has no halo tail owing to its large angular momentum. The wave function of the $4_1^+ \otimes f_{7/2}$ channel dumps as rapidly as that of the $2_1^+ \otimes f_{7/2}$ channel, although it is not shown in the figure.

The resonance energies and widths calculated using the ACCC are shown in Fig. 4 and Table II. The S factors of the resonances are calculated at the bound region close to $\lambda = \lambda_0$ because the S factors at the physical point cannot be calculated within the ACCC framework. It is found that the S factors are not sensitive to the value of λ in the vicinity of $\lambda = \lambda_0$; hence we expect that these values are a reasonable approximation of the S factors at the physical point.

The S factor shows us the structure of the resonances. The first excited state is the $5/2_1^-$ state for which the $0_1^+ \otimes p_{3/2}$

TABLE II. One-neutron separation energy and widths in units of MeV, and the S factors of the ground and excited states of ^{31}Ne calculated using AMD+RGM and ACCC. The S factors of the resonances are calculated at the bound region close to $\lambda = \lambda_0$. The numbers in the parentheses are the resonance energies obtained within the bound-state approximation. The results of the AMD+GCM are also shown for the ground state.

	S_n	Γ	$0_1^+ \otimes p_{3/2}$	$2_1^+ \otimes p_{3/2}$	$4_1^+ \otimes p_{3/2}$	$0_1^+ \otimes f_{7/2}$	$2_1^+ \otimes f_{7/2}$	$4_1^+ \otimes f_{7/2}$
$3/2_1^-$(GCM)	−0.36		0.13	0.32			0.78	0.66
$3/2_1^-$(RGM)	0.61		0.30	0.43			0.57	0.47
$5/2_1^-$	−0.12 (−0.12)	0.07		0.48	0.12		0.66	0.33
$7/2_1^-$	−0.69 (−0.60)	0.18		0.07	0.21	0.76	0.05	0.06
	S_n	Γ	$0_2^+ \otimes p_{3/2}$	$2_2^+ \otimes p_{3/2}$	$0_2^+ \otimes f_{7/2}$	$2_2^+ \otimes f_{7/2}$		
$3/2_2^-$	−1.76 (−1.02)	0.29	0.64	0.09		0.23		
$7/2_2^-$	−1.60 (−1.22)	0.21		0.14	0.65	0.14		

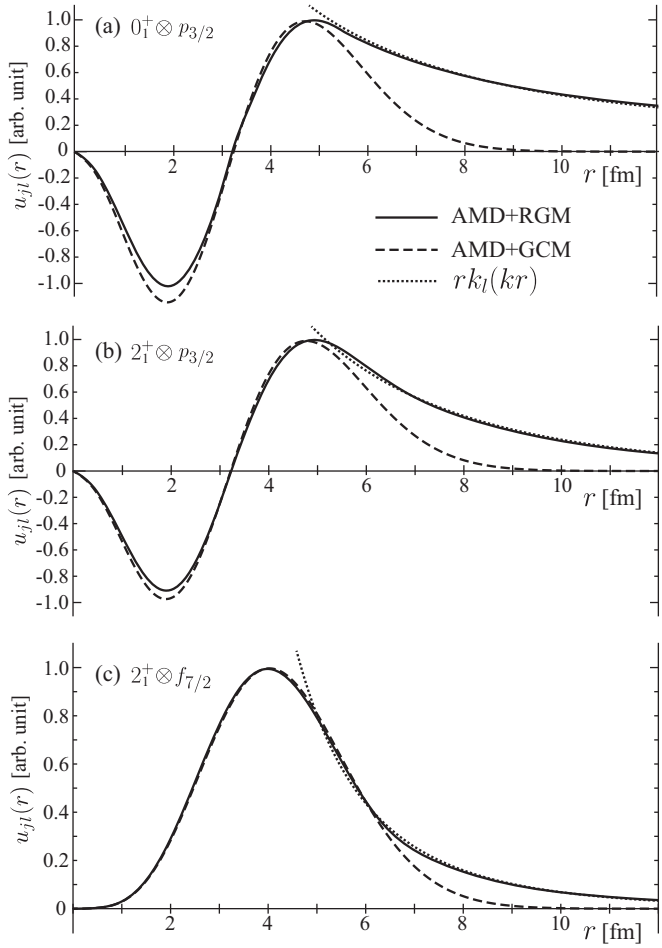

FIG. 5. Wave functions (overlap functions) of the ground state of ^{31}Ne in the (a) $0_1^+ \otimes p_{3/2}$, (b) $2_1^+ \otimes p_{3/2}(2_1^+)$, and (c) $2_1^+ \otimes f_{7/2}(2_1^+)$ channels calculated using the AMD+GCM and AMD+RGM. The amplitudes are arbitrarily normalized for presentation. The dotted lines show the correct asymptotics at large distances, where the interaction between ^{30}Ne and the valence neutron is negligible.

channel is forbidden and the core-excited $2_1^+ \otimes p_{3/2}$ and $2_1^+ \otimes f_{7/2}$ channels dominate. Therefore, we regard this state as the rotational excitation of the ^{30}Ne core coupled to the neutron halo with p- and f-wave mixing. We have also calculated the S factor for the $0_1^+ \otimes f_{5/2}$ channel and found it to be very small. Note that this state is located above the $^{30}\mathrm{Ne}(0_1^+) + n$ threshold but below the $^{30}\mathrm{Ne}(2_1^+) + n$ threshold; hence, the decay channel of the main component is closed. Consequently, this state is a narrow and sharp resonance. The $7/2_1^-$ state looks like a rotational state in the sequence of the $3/2_1^-$, $5/2_1^-$, and $7/2_1^-$ states. However, the S factor indicates that this state is a single-particle state, that is, it is dominated by the $0_1^+ \otimes f_{7/2}$ component. Because the decay channel is open, its width is larger than that of the $5/2_1^-$ state. We also note that the energy of these resonances ($5/2_1^-$ and $7/2_1^-$) can be reasonably evaluated within the bound state approximation because their energies are not much higher than the decay threshold.

The $3/2_2^-$ and $7/2_2^-$ states are significantly different from the other states. They are strongly coupled to the spherical $^{30}\mathrm{Ne}(0_2^+)$ with the $0\hbar\omega$ configuration. Owing to small deformation, the coupling to $^{30}\mathrm{Ne}(2_2^+)$ is not strong. It decays through weakly coupled $^{30}\mathrm{Ne}(0_1^+)$ channels, and the widths are broader due to larger decay Q values. For these resonances, the bound state approximation yields inaccurate estimation of the resonance energy due to the contamination of non-resonant continua. The structure of this state is considerably different from the ground state of ^{31}Ne and the neighboring nuclei, indicating the coexistence of the deformed halo state and spherical non-halo states.

Finally, we compare our numerical results with the latest experimental data obtained by the two-proton knockout reaction from ^{33}Mg [31]. They observed two low-lying peaks at 0.30 ± 0.17 and 1.50 ± 0.33 MeV in the $^{30}\mathrm{Ne} + n$ decay spectrum, which might correspond to either two resonances or two groups of resonances. Since they did not observe the final state of ^{30}Ne, there are two interpretations of the data. If we assume the decay to the ground state of ^{30}Ne, the corresponding one-neutron separation energies are 0.30 and 1.50 MeV for the lower and higher peaks, respectively. This interpretation is qualitatively consistent with our results: the lower peak ($S_n = 0.30$ MeV) corresponds to the $5/2_1^-$ and $7/2_1^-$ states, while the higher peak ($S_n = 1.50$ MeV) can be assigned to the $3/2_1^-$ and $7/2_1^-$ states. The higher peak is broader than the lower peak, which also qualitatively agrees with our results.

Another interpretation of the data is the assumption of the decay to the 2_1^+ state of ^{30}Ne. In this case, the lower and higher peaks correspond to $S_n = 1.1$ and 2.3 MeV, respectively. This interpretation is less consistent with our results. In particular, we have not obtained the resonances corresponding to $S_n = 2.3$ MeV. Note that this does not mean that such resonances do not exist, but we could not obtain the numerical results in this energy region because of the lack of the numerical precision of the ACCC calculation. In any case, further theoretical and experimental studies are needed to identify the ^{31}Ne resonances, which is a quite interesting issue.

IV. SUMMARY

In this study, we have discussed the properties of the deformed halo of ^{31}Ne by applying the AMD+RGM and investigated the properties of the resonances built on top of the ground state by applying the ACCC. By comparing the results from the conventional AMD+GCM framework, we have shown that the AMD+RGM correctly describes the asymptotic form of the neutron halo wave function and yields a large neutron radius for ^{31}Ne. We have also microscopically calculated the S factors, revealing that the ground state of ^{31}Ne is dominated by core-excited channels ($2^+ \otimes p_{3/2}$ and $2^+ \otimes f_{7/2}$) rather than the ground-state channel. This result explains the observed S factor in the ground-state channel, 0.32 ± 0.21, reported by a one-neutron removal experiment [11]. Simultaneously, it shows that ^{31}Ne is a deformed halo nucleus in which the rotational excitation of the core is coupled with a deformed neutron halo.

Furthermore, by applying the ACCC to the AMD+RGM, the energy and width of the resonances have been obtained. The first excited state, the $5/2^-$ state, is dominated by core-excited components. Because neutron decay in the dominant

channel is a negative Q value, this state has a small width. In contrast, the second excited state, the $7/2^-_1$ state, is dominated by the $f_{7/2}$ channel. Other obtained resonances are predicted to have the valence neutron coupled to the spherical 0^+_2 state of ^{30}Ne.

We have also compared our results with the latest experimental data [31]. Although quantitative comparison is difficult due to the uncertainty of the experiment, we have confirmed that the observed candidate of resonances are qualitatively consistent with our results, assuming that the decays to the ground state of ^{30}Ne were observed in the experiment.

We note that the successful combination of the AMD+RGM and ACCC frameworks will allow us to discuss the properties of other deformed haloes, such as ^{37}Mg, and the nuclei beyond the neutron drip line, such as ^{26}O.

ACKNOWLEDGMENTS

This work was supported by the Collaborative Research Program 2022 at Hokkaido University, and JSPS KAKENHI Grants No. 18K03635, No. 19K03859, No. 21H00113, and No. 22H01214.

[1] I. Tanihata, J. Phys. G: Nucl. Part. Phys. **22**, 157 (1996).
[2] I. Tanihata, H. Hamagaki, O. Hashimoto, Y. Shida, N. Yoshikawa, K. Sugimoto, O. Yamakawa, T. Kobayashi, and N. Takahashi, Phys. Rev. Lett. **55**, 2676 (1985).
[3] W. Horiuchi and Y. Suzuki, Phys. Rev. C **74**, 034311 (2006).
[4] K. Tanaka, T. Yamaguchi, T. Suzuki, T. Ohtsubo, M. Fukuda, D. Nishimura, M. Takechi, K. Ogata, A. Ozawa, T. Izumikawa, T. Aiba, N. Aoi, H. Baba, Y. Hashizume, K. Inafuku, N. Iwasa, K. Kobayashi, M. Komuro, Y. Kondo, T. Kubo *et al.*, Phys. Rev. Lett. **104**, 062701 (2010).
[5] W. Horiuchi, T. Inakura, T. Nakatsukasa, and Y. Suzuki, Phys. Rev. C **86**, 024614 (2012).
[6] N. Kobayashi, T. Nakamura, Y. Kondo, J. A. Tostevin, Y. Utsuno, N. Aoi, H. Baba, R. Barthelemy, M. A. Famiano, N. Fukuda, N. Inabe, M. Ishihara, R. Kanungo, S. Kim, T. Kubo, G. S. Lee, H. Lee, M. Matsushita, T. Motobayashi, T. Ohnishi, N. A. Orr, H. Otsu, T. Otsuka, T. Sako, H. Sakurai, Y. Satou, T. Sumikama, H. Takeda, S. Takeuchi, R. Tanaka, Y. Togano, and K. Yoneda, Phys. Rev. Lett. **112**, 242501 (2014).
[7] M. Takechi, S. Suzuki, D. Nishimura, M. Fukuda, T. Ohtsubo, M. Nagashima, T. Suzuki, T. Yamaguchi, A. Ozawa, T. Moriguchi, H. Ohishi, T. Sumikama, H. Geissel, N. Aoi, R.-J. Chen, D.-Q. Fang, N. Fukuda, S. Fukuoka, H. Furuki, N. Inabe *et al.*, Phys. Rev. C **90**, 061305 (2014).
[8] S. Bagchi, R. Kanungo, Y. K. Tanaka, H. Geissel, P. Doornenbal, W. Horiuchi, G. Hagen, T. Suzuki, N. Tsunoda, D. Ahn, H. Baba, K. Behr, F. Browne, S. Chen, M. Cortés, A. Estradé, N. Fukuda, M. Holl, K. Itahashi, N. Iwasa, G. R. Jansen, W. G. Jiang, S. Kaur, A. O. Macchiavelli, S. Y. Matsumoto, S. Momiyama, I. Murray, T. Nakamura, S. J. Novario, H. J. Ong, T. Otsuka, T. Papenbrock, S. Paschalis, A. Prochazka, C. Scheidenberger, P. Schrock, Y. Shimizu, D. Steppenbeck, H. Sakurai, D. Suzuki, H. Suzuki, M. Takechi, H. Takeda, S. Takeuchi, R. Taniuchi, K. Wimmer, and K. Yoshida, Phys. Rev. Lett. **124**, 222504 (2020).
[9] M. Takechi, T. Ohtsubo, M. Fukuda, D. Nishimura, T. Kuboki, T. Suzuki, T. Yamaguchi, A. Ozawa, T. Moriguchi, H. Ooishi, D. Nagae, H. Suzuki, S. Suzuki, T. Izumikawa, T. Sumikama, M. Ishihara, H. Geissel, N. Aoi, R.-J. Chen, D.-Q. Fang *et al.*, Phys. Lett. B **707**, 357 (2012).
[10] T. Nakamura, N. Kobayashi, Y. Kondo, Y. Satou, N. Aoi, H. Baba, S. Deguchi, N. Fukuda, J. Gibelin, N. Inabe, M. Ishihara, D. Kameda, Y. Kawada, T. Kubo, K. Kusaka, A. Mengoni, T. Motobayashi, T. Ohnishi, M. Ohtake, N. A. Orr *et al.*, Phys. Rev. Lett. **103**, 262501 (2009).
[11] T. Nakamura, N. Kobayashi, Y. Kondo, Y. Satou, J. A. Tostevin, Y. Utsuno, N. Aoi, H. Baba, N. Fukuda, J. Gibelin, N. Inabe, M. Ishihara, D. Kameda, T. Kubo, T. Motobayashi, T. Ohnishi, N. A. Orr, H. Otsu, T. Otsuka, H. Sakurai *et al.*, Phys. Rev. Lett. **112**, 142501 (2014).
[12] K. Riisager, A. Jensen, and P. Møller, Nucl. Phys. A **548**, 393 (1992).
[13] I. Hamamoto, Phys. Rev. C **81**, 021304(R) (2010).
[14] A. Poves and J. Retamosa, Nucl. Phys. A **571**, 221 (1994).
[15] Y. Urata, K. Hagino, and H. Sagawa, Phys. Rev. C **83**, 041303(R) (2011).
[16] Y. Urata, K. Hagino, and H. Sagawa, Phys. Rev. C **86**, 044613 (2012).
[17] K. Minomo, T. Sumi, M. Kimura, K. Ogata, Y. R. Shimizu, and M. Yahiro, Phys. Rev. C **84**034602 (2011).
[18] K. Minomo, T. Sumi, M. Kimura, K. Ogata, Y. R. Shimizu, and M. Yahiro, Phys. Rev. Lett. **108**, 052503 (2012).
[19] T. Sumi, K. Minomo, S. Tagami, M. Kimura, T. Matsumoto, K. Ogata, Y. R. Shimizu, and M. Yahiro, Phys. Rev. C **85**064613 (2012).
[20] V. I. Kukulin and V. M. Krasnopol'sky, J. Phys. A: Math. Gen. **10**, L33 (1977).
[21] N. Tanaka, Y. Suzuki, and K. Varga, Phys. Rev. C **56**, 562 (1997).
[22] J. F. Berger, M. Girod, and D. Gogny, Comput. Phys. Commun. **63**, 365 (1991).
[23] M. Kimura, Phys. Rev. C **69**, 044319 (2004).
[24] D. L. Hill and J. A. Wheeler, Phys. Rev. **89**, 1102 (1953).
[25] Y. Kanada-En'yo, M. Kimura, and H. Horiuchi, C. R. Phys. **4**, 497 (2003).
[26] Y. Kanada-En'yo, M. Kimura, and A. Ono, Prog. Theor. Exp. Phys. **2012**, 1A202 (2012).
[27] M. Kimura, T. Suhara, and Y. Kanada-En'yo, Eur. Phys. J. A **52**, 373 (2016).
[28] M. Dan, R. Chatterjee, and M. Kimura, Eur. Phys. J. A **57**, 203 (2021).
[29] E. Chabanat, P. Bonche, P. Haensel, J. Meyer, and R. Schaeffer, Nucl. Phys. A **627**, 710 (1997).
[30] M. Kimura, Phys. Rev. C **95**, 034331 (2017).
[31] D. Chrisman, A. N. Kuchera, T. Baumann, A. Blake, B. A. Brown, J. Brown, C. Cochran, P. A. DeYoung, J. E. Finck, N. Frank, P. Guèye, H. Karrick, H. Liu, J. McDonaugh, T. Mix, B. Monteagudo, T. H. Redpath, W. F. Rogers, R. Seaton-Todd, A. Spyrou *et al.*, Phys. Rev. C **104**, 034313 (2021).